Chemical Engineering Journal 302 (2016) 577–586

Contents lists available at ScienceDirect

Chemical Engineering Journal

journal homepage: www.elsevier.com/locate/cej

Layered hydroxyl sulfate: Controlled crystallization, structure analysis, and green derivation of multi-color luminescent $(La,RE)_2O_2SO_4$ and $(La,RE)_2O_2S$ phosphors (RE = Pr, Sm, Eu, Tb, and Dy)

Xuejiao Wang [a,b], Ji-Guang Li [a,b,*], Maxim S. Molokeev [c,d], Qi Zhu [a], Xiaodong Li [a], Xudong Sun [a]

[a] Key Laboratory for Anisotropy and Texture of Materials (Ministry of Education), School of Materials Science and Engineering, Northeastern University, Shenyang, Liaoning 110819, China
[b] Advanced Materials Processing Unit, National Institute for Materials Science, Tsukuba, Ibaraki 305-0044, Japan
[c] Laboratory of Crystal Physics, Kirensky Institute of Physics, SB RAS, Krasnoyarsk 660036, Russia
[d] Department of Physics, Far Eastern State Transport University, Khabarovsk 680021, Russia

HIGHLIGHTS

- Formation window of layered $La_2(OH)_4SO_4{\cdot}nH_2O$ was defined.
- Oxysulfate and oxysulfide were facilely derived from the layered compound.
- Crystal structures of $La_2(OH)_4SO_4{\cdot}nH_2O$, oxysulfate and oxysulfide were deciphered.
- Multi-color photoluminescence was achieved in oxysulfate and oxysulfide.
- Concentration and host dependent luminescence was well addressed.

GRAPHICAL ABSTRACT

The formation window and crystal structure of $La_2(OH)_4SO_4{\cdot}2H_2O$ (La-241) layered hydroxide were originally reported. Rare-earth (Pr^{3+}, Sm^{3+}, Eu^{3+}, Tb^{3+}, and Dy^{3+}) doped oxysulfate and oxysulfide phosphors were also successfully derived with (La,RE)-241 as a green precursor for multi-color photoluminescence.

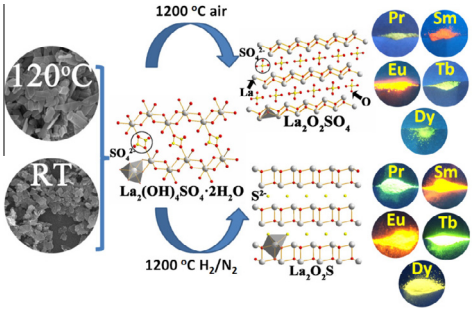

ARTICLE INFO

Article history:
Received 7 April 2016
Received in revised form 12 May 2016
Accepted 20 May 2016
Available online 20 May 2016

Keywords:
Sulfate type layered rare earth hydroxide
Photoluminescence
Oxysulfate
Oxysulfide

ABSTRACT

The two important groups of $Ln_2O_2SO_4$ and Ln_2O_2S compounds are traditionally synthesized with the involvements of environmentally harmful sulfur-containing reagents. We developed in this work a unique green approach for their synthesis, using $Ln_2(OH)_4SO_4{\cdot}2H_2O$ layered hydroxyl sulfate as the precursor (Ln-241 phase). Phase selective crystallization of La-241 under both atmospheric pressure and hydrothermal conditions was firstly optimized, followed by transformation into La_2O_2S and $La_2O_2SO_4$ by controlled calcination. Rietveld structure refinement was performed for La-241, $La(OH)SO_4$, $La_2O_2SO_4$, and La_2O_2S, and the crystal structure and cell parameters of La-241 were originally reported. The photoluminescence performances of several important activators (Pr^{3+}, Sm^{3+}, Eu^{3+}, Tb^{3+}, and Dy^{3+}) in the two hosts, in terms of excitation, emission, quantum yield, and color coordinates of emission, were thoroughly investigated, and multi-color luminescence including bright red, green, orange red, and yellow was obtained under ultraviolet excitation. Detailed investigations of Tb^{3+} photoluminescence revealed that the lack of $^5D_3$ emission in La_2O_2S and the gradual quenching of $^5D_3$ blue emission at a higher Tb^{3+} content (hence decreasing I_{488}/I_{545} ratio and changing color coordinates) in $La_2O_2SO_4$ were suggested to be due to thermal activation of the $^5D_3$ electrons into the conduction band and cross

* Corresponding author at: National Institute for Materials Science, Japan.
E-mail address: LI.Jiguang@nims.go.jp (J.-G. Li).

http://dx.doi.org/10.1016/j.cej.2016.05.089

relaxation between adjacent Tb^{3+}, respectively. The synthesis approach developed in this work for $La_2O_2SO_4$ and La_2O_2S, with water vapor as the only exhaust gas, is environmentally benign and holds great potential in the facile synthesis of analogous compounds of other lanthanides.

1. Introduction

The layered rare-earth hydroxides (LRHs) of $Ln_2(OH)_{6-m}(A^{x-})_{m/x}\cdot nH_2O$ (Ln: trivalent rare-earth ion; A: guest anion; $1.0 \leqslant m \leqslant 2.0$) have been drawing keen research interest during the recent years due to their unique combination of the fascinating layered crystal structure and the multi-functionalities of the Ln elements [1–4]. The LRHs can be classified into the two major categories of $Ln_2(OH)_5(A^{x-})_{1/x}\cdot nH_2O$ ($m = 1$) and $Ln_2(OH)_4(A^{x-})_{2/x}\cdot nH_2O$ ($m = 2$) according to chemical composition and structural features [5]. The crystal structure of the first group is analogous to the well-known anion-exchangeable material of layered double hydroxide (LDH), which attracts much interest in recent years and finds applications in various fields including flame retardants, hydrogel, UV-ray shielding, and tunable photoluminescence et al. [6–11]. Extensive efforts have been paid to this category of LRHs since its first report in 2006, in terms of synthesis, structure characterization, anion exchange, exfoliation, and optical functionalization [3,12–14]. Reports on the compounds that belong to the second group, where the A anion is monovalent (such as Cl^-, Br^-, or NO_3^-; $Ln(OH)_2A\cdot nH_2O$), can be dated back to 1970s [15,16] but only until recently their layered nature was unveiled [17,18].

Enormous potential applications and interesting properties of the LRHs inspire researchers to design new compositions. Sasaki et al. [5] reported in 2010 a new group of LRHs belonging to the second category, that is, $Ln_2(OH)_4SO_4\cdot nH_2O$ (Ln = Pr–Tb, hereafter referred to Ln-241 phase). Different from the spherical coordination of halide and the planar coordination of nitrate, the bivalent sulfate anion assumes a tetrahedral geometry (T_d point symmetry), and thus the compounds differ in structure, cation coordination and property from the aforesaid $Ln_2(OH)_5(A^{x-})_{1/x}\cdot nH_2O$ ($m = 1$) and $Ln(OH)_2A\cdot nH_2O$. It is delighted to notice that this new group of layered compounds has exactly the Ln/S atomic ratio of Ln_2O_2S and $Ln_2O_2SO_4$, two types of important materials for luminescence and redox (such as oxygen storage) applications [19–24]. It is thus expected that Ln-241 can serve as an ideal precursor to yield Ln_2O_2S and $Ln_2O_2SO_4$ via simple dehydration and dehydroxylation under controlled calcination. The conceived technical route, having water vapor as the only exhaust gas, would be significantly superior to traditional synthesis, which generally involves the environmentally harmful sulfur-containing materials of thiourea, S, CS_2, H_2S, and SO_x [25–28]. Up to date, the studies on Ln-241 are limited to the Ln of Pr–Tb, and materials synthesis was largely performed via homogeneous hydrolysis of sulfate salts in the presence of hexamethylenetetramine (HMT) under ambient pressure [5]. Lanthanide contraction predicts that the crystallization behaviors of 241 analogues differ in various aspects for different Ln, and it is thus of particular scientific interest to investigate material synthesis, structure, and functionalization of the compounds for the Ln beyond the above reported range.

This work exemplifies the crystallization of $La_2(OH)_4SO_4\cdot 2H_2O$ (La-241) via reaction of lanthanum nitrate with ammonium sulfate ($(NH_4)_2SO_4$) under both atmospheric pressure and hydrothermal conditions, and functionalization of the annealing-derived optically inert La_2O_2S and $La_2O_2SO_4$ lattices with rare-earth activators (Pr^{3+}, Sm^{3+}, Eu^{3+}, Tb^{3+}, and Dy^{3+}) for multi-color photoluminescence. The effects of reaction temperature (RT-200 °C) on phase structure of the product were investigated in detail and the formation window of La-241 was defined. For the first time, the crystallographic data of La-241 were resolved via Rietveld refinement and presented. Photoluminescence properties of the aforementioned activators in both La_2O_2S and $La_2O_2SO_4$ were discussed in detail, and concentration-dependent PL properties were further studied with Tb^{3+} for example.

2. Experimental

2.1. Materials and synthesis

The starting materials of $Ln(NO_3)_3\cdot 6H_2O$ (Ln = La, Pr, Sm, Eu, Tb, and Dy, >99.99% pure), $(NH_4)_2SO_4$ (>99.5% pure), and $NH_3\cdot H_2O$ solution (ultrahigh purity) were purchased from Kanto Chemical Co., Inc. (Tokyo, Japan) and were used as received. Milli-Q filtered water (resistivity ~ 18 MΩ cm) was used throughout the experiment. In a typical synthesis, 6 mmol of $(NH_4)_2SO_4$ was dissolved in 60 ml of La^{3+} solution (0.1 mol/L), and then $NH_3\cdot H_2O$ was dropwise added until pH ~ 9 after continuous stirring for 15 min. The resultant suspension was either kept under ambient pressure at a prescribed temperature (with magnetic stirring) for 24 h or transferred into a Teflon lined autoclave of 100 ml for 24 h of hydrothermal crystallization in a preheated air oven (without stirring). The resultant product was collected via centrifugation, washed with water three times, ethanol once, and finally dried in air at 70 °C for 24 h. The activator (Pr^{3+}, Sm^{3+}, Eu^{3+}, Tb^{3+}, and Dy^{3+}) doped La-241 samples were synthesized in a similar way at the optimized hydrothermal temperature of 100 °C. Oxysulfate and oxysulfide powders were then annealed from their hydroxyl sulfate precursors in air and N_2/H_2 gas mixture (95/5 in volume; flowing at 200 ml/min) at 1200 °C for 1 h, respectively, with a heating rate of 5 °C/min in the ramp stage. Though the optimal concentration of Eu^{3+} in oxysulfate and oxysulfide phosphors may reach 5 at.% [25,29], those for Pr^{3+}, Sm^{3+}, and Dy^{3+} in oxysulfide are generally limited to ~1 at.% [30–32]. As for Tb^{3+}, the occurrence of emission from the $^5D_3$ excited state is known to widely vary among hosts and the emission intensity is significantly affected by Tb^{3+} content [33]. We thus adopted in this work the same activator content of 1 at.% for Eu^{3+}, Pr^{3+}, Sm^{3+}, and Dy^{3+} to illustrate the excitation/emission behaviors and meanwhile varying Tb^{3+} content to study concentration dependent photoluminescence (PL).

2.2. Characterizations

Phase identification was performed via X-ray diffractometry (XRD; Model RINT2200, Rigaku, Tokyo, Japan) operated at 40 kV, 40 mA using nickel-filtered Cu-$K\alpha$ radiation (0.15406 nm) and a scanning speed of 1°/min. The powder XRD for Rietveld refinement was measured in a step-scan mode with a step size of 0.02° and an accumulation time of 35 s. Morphologies of the products were observed by field emission scanning electron microscopy (FE-SEM; Model S-5000, Hitachi, Tokyo) operated at 10 kV. Rietveld refinement was carried out using the TOPAS 4.2 software [34,35]. The functional groups built in the molecules of the products were investigated using Fourier transform infrared spectroscopy (FTIR; Model 4200, JASCO, Tokyo) by the standard KBr method. Photoluminescence was measured on an FP-6500 fluorospectrophotometer (JASCO) equipped with a 150 W xenon lamp

as the excitation source. All the measurements were conducted under identical instrumental settings, with a scanning speed of 100 nm/min, a slit width of 3 nm for both excitation and emission, and a signal to noise ratio (S/N) of ⩾200. The efficiency of luminescence was measured by an absolute PL quantum yield (QY) measurement system (C9920-02, Hamamatsu Photonics K.K., Kanagawa, Japan), which consists of a xenon lamp excitation source, a monochromator, an integrating sphere capable of nitrogen gas flow, and a CCD detector working for the whole measured spectral range. Light absorption of the activator-free oxysulfate ($La_2O_2SO_4$) and oxysulfide (La_2O_2S) was studied via UV–vis spectroscopy (Model V-560, JASCO). Particle size of the typical oxysulfate and oxysulfide phosphors was analyzed by laser diffraction particle sizing (LDPS; Model Horiba LA-920, Kyoto, Japan). All the above analyses were performed at room temperature.

3. Results and discussion

3.1. Controlled synthesis of La-based compounds and structure analysis

Fig. 1 shows XRD patterns of the products crystallized at various temperatures (from RT to 200 °C). It was found that the peaks recorded from the products synthesized in the RT-120 °C range can all be indexed to $La_2(OH)_4SO_4{\cdot}2H_2O$ (La-241), which is verified by Rietveld refinement. Intensity ratio of the (200) to (111) diffractions increased from 0.45 to 2.50 as the synthesis temperature increased from RT to 120 °C. This phenomenon is originated from the peculiar growth habit of the layered compound and also closely related to morphology change of the crystallites in response to synthesis temperature. The La-241 phase crystalizes in a monoclinic unit cell, and the structure is built up via alternative stacking of sulfate ions and the [LaO_9] polyhedra containing two-dimensional host layers along the *a*-axis. Thus, non-(*h*00) diffractions (such as (111)) reflect structural features of the host layer while (*h*00) diffractions reflect stacking of the host layer along the *a*-axis. A higher reaction temperature produces thicker plates for the product, and thus substantially stronger (200) diffraction

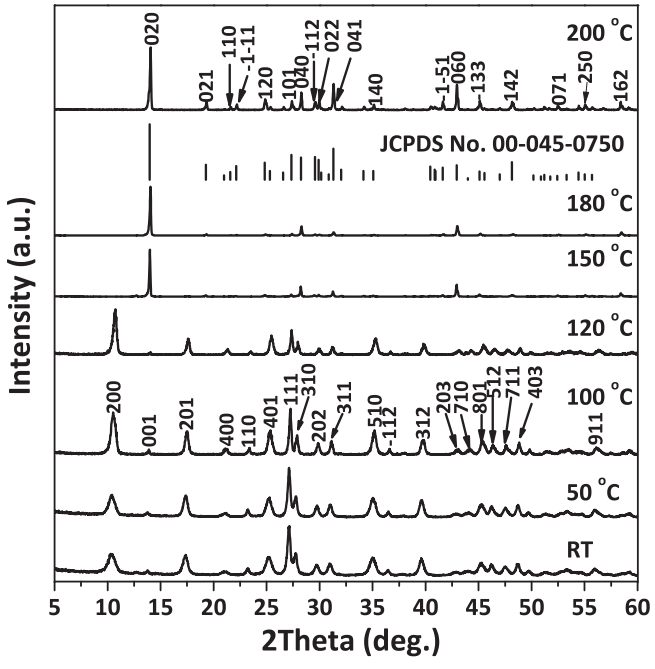

Fig. 1. XRD patterns of the $La_2(OH)_4SO_4{\cdot}2H_2O$ (La-241, RT-120 °C), $La(OH)SO_4$ (150–180 °C, with trace impurity), and $La(OH)SO_4$ (200 °C) products.

was observed. Gallery height (1/2*a*sinβ) of the layered structure is thus closely related to the position of the (200) diffraction, which was calculated with the refinement results to be ~8.442 Å for the 100 °C sample. Both the 150 and 180 °C products were identified to be anhydrous $La(OH)SO_4$ (La-111) with trace impurity as seen from the enlarged XRD patterns (Fig. S1). Further raising the reaction temperature to 200 °C led to crystallization of La-111 as a pure phase (Fig. 1).

Fig. 2 displays FE-SEM morphologies of the La-241 phase crystallized at different temperatures. As seen, increasing temperature of crystallization promotes crystallite growth, changing the plates from 200 to 300 nm in lateral and 20–30 nm in thickness for the RT product (Fig. 2(a)) to 700–1100 nm in lateral and 40–70 nm in thickness for the 120 °C one (Fig. 2(d)). Such a micromorphology evolution agrees well with intensity evolution of the (200) diffraction and the altered (200)/(111) intensity ratio (Fig. 1). Two kinds of distinctly different morphologies were found for the 150 °C product (Fig. 2(e)). The results of XRD suggest that the smaller nanoplates and the microplates (~100 μm) correspond to the impurity and La-111 phases, respectively, as the latter dominates phase constituent of the product. The impurity nanoplates vanished from the 200 °C product (Fig. 2(f)), conforming to crystallization of La-111 as a pure phase though the particles are not uniform in size.

Fig. 3 shows FTIR spectra for five representative samples. As identical IR responses were observed for the 100 and 120 °C products, the later was analyzed in detail for example. The vibrations at ~3251 and 1676 cm^{-1} can be attributed to the O–H stretching vibrations (v_1 and v_3) and the H–O–H bending mode (v_2) of hydration water in the structure, respectively, while the absorptions at ~532 and 765 cm^{-1} are originated from the bending modes of water molecules coordinated to metal ions [5,36]. The two separated sharp bands located at ~3604 and 3478 cm^{-1} can be assigned to hydroxyl (OH^-) groups [36]. Compared with anhydrous $La(OH)SO_4$, the additional OH^- vibration resolved at ~3604 cm^{-1} for $La_2(OH)_4SO_4{\cdot}2H_2O$ was believed to arise from intra-molecular H_2O/SO_4^{2-} interactions via hydrogen bonding, since the coupling distorts the molecular structure of H_2O and thus additional hydroxyl absorption appears [21]. The v_1, v_2, v_3, and v_4 fundamental vibrations of sulfate groups were all observed as labeled in the figure, with the v_3 and v_4 spilt into several peaks. The 150–200 °C products similarly present well-resolved hydroxyl (~3489 and 823 cm^{-1}) and sulfate absorptions but essentially no water vibration, conforming to the intrinsically anhydrous nature of the La-111 compound identified via XRD (Fig. 1). For the sulfate bands of La-111, the v_1 and v_4 vibrations are clearly significantly stronger, along with extending of v_3 from ~1250 to 1040 cm^{-1} for the 100 and 120 °C products to the wider range of ~1310–1030 cm^{-1}. These indicate that the phase transition from La-241 to La-111 changes SO_4^{2-} coordination and aggravates distortion of the SO_4^{2-} tetrahedrons. To quantitatively characterize the distortion, a polyhedral distortion index (D) was introduced as follows [37,38],

$$D = (1/n)\sum(|l_i - l_{av}|/l_{av}) \quad (1)$$

where l_i is the distance from the central sulfur atom to the *i*th coordinating oxygen (*i* = 1–4) and l_{av} is the average S–O bond length. It was found that the *D* value of 0.011 for the SO_4^{2-} in La-241 is only one fourth that (*D* = 0.040) of the SO_4^{2-} in La-111. That is, substantially higher distortion of [SO_4] tetrahedron in the latter. The reason is the different site symmetry of the S atom, which is *m* (C_s) in La-241 (4*i* Wyckoff site) while 1 (C_1) in La-111 (4*e* Wyckoff site). That is, absence of any symmetry element in the latter.

As the 100 °C La-241 product has already shown well-developed hydroxide main layers and interlayer gallery, it was thus used to derive oxysulfide and oxysulfate via calcination. Fig. 4

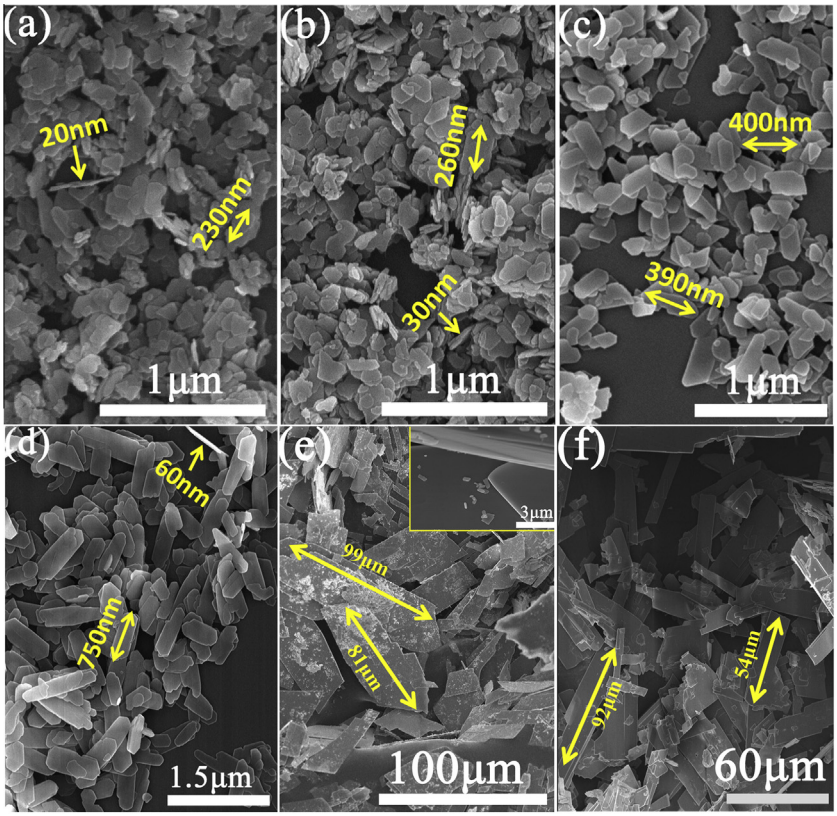

Fig. 2. FE-SEM images of the products crystallized at the different temperatures of RT (a), 50 (b), 100 (c), 120 (d), 150 (e), and 200 °C (f).

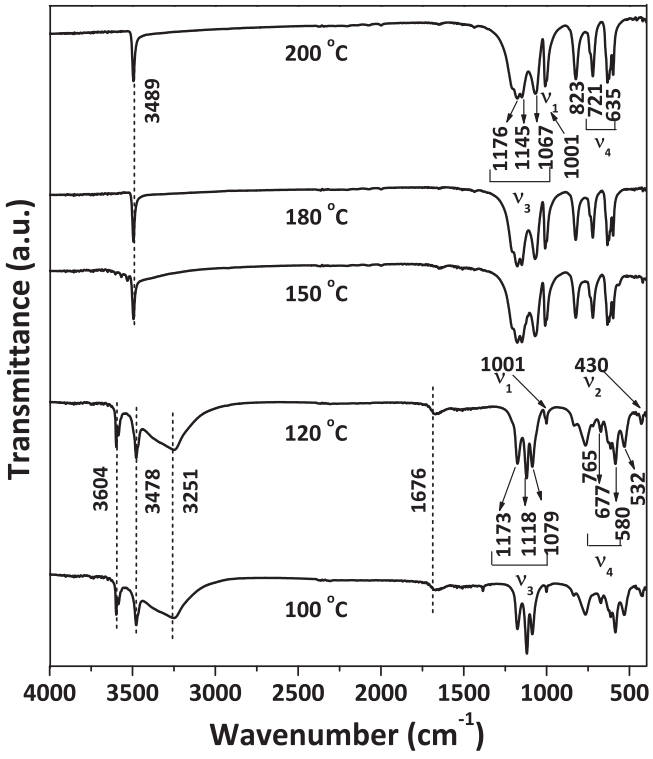

Fig. 3. FTIR spectra of $La_2(OH)_4SO_4{\cdot}2H_2O$ (La-241, 100–120 °C), $La(OH)SO_4$ with trace impurity (150–180 °C), and pure $La(OH)SO_4$ (200 °C).

exhibits XRD patterns of the La-241 precursor and the products calcined at 1200 °C, where it is seen that both $La_2O_2SO_4$ and La_2O_2S were resulted as pure phases by annealing in air and N_2/H_2 gas mixture, respectively. The oxysulfate compound was formed via simple dehydration and dehydroxylation of La-241 (Eqs. (2) and (3)) as reported for the Pr–Tb analogues [5], while in N_2/H_2 gas mixture the H_2 component may take out oxygen atoms from $La_2O_2SO_4$ and concomitantly reduce S^{6+} to S^{2-} at high temperatures to yield La_2O_2S (Eq. (4)).

$$La_2(OH)_4SO_4 \cdot 2H_2O \rightarrow La_2(OH)_4SO_4 + 2H_2O \quad (2)$$

$$La_2(OH)_4SO_4 \rightarrow La_2O_2SO_4 + 2H_2O \quad (3)$$

$$La_2O_2SO_4 + 4H_2 \rightarrow La_2O_2S + 4H_2O \quad (4)$$

Since the structural parameters of La-241 has not been reported so far and the studies on $La(OH)SO_4$ are rather limited, we thus carried out comprehensive Rietveld structure refinements for the two compounds (Fig. 5(a) and (b)), using the crystallographic data of their rare-earth analogues as initial structure models [39,40]. All the XRD peaks of $La_2(OH)_4SO_4{\cdot}2H_2O$ were found to be indexable with the monoclinic cell ($A2/m$) of $Tb_2(OH)_4SO_4{\cdot}2H_2O$ [39], and the crystal structure was further transformed into space group $C2/m$ to get standard settings. After refinements, we found that La-241 is isostructural to its reported Pr–Tb counterparts [39], but with lager cell parameters and cell volume. It should be noted that the exact positions of H atoms in the structure have not been definitely determined in this work, since the H atoms are disordered together with SO_4^{2-} in at least two positions and thus only the possible region of H atom is proposed (Fig. S2). The powder XRD pattern of $La(OH)SO_4$ can be indexed by a monoclinic cell ($P2_1/n$) with parameters close to $Pr(OH)SO_4$ [40], and the H atom in hydroxyl is positioned as riding on the O parent atom. In addition, Rietveld refinements of $La_2O_2SO_4$ and La_2O_2S diffractions with the already existing crystal structures [41,42] yielded good fitting

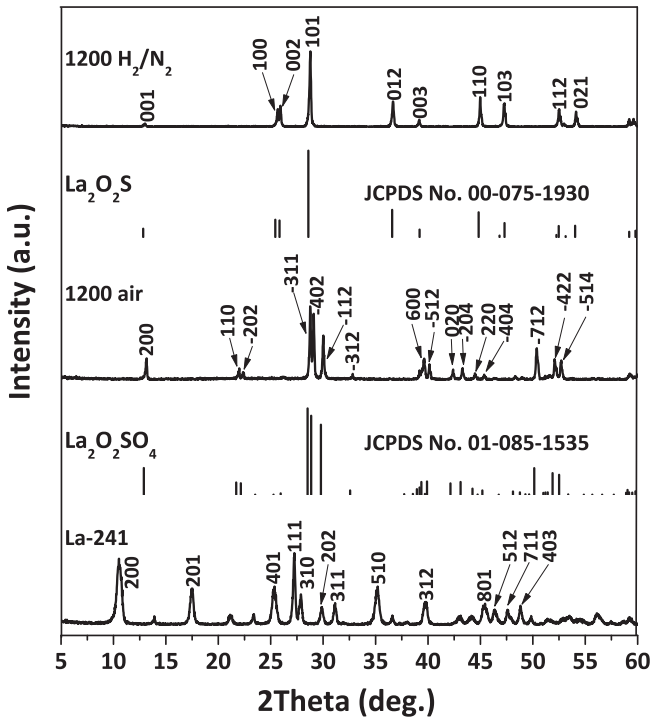

Fig. 4. XRD patterns of the La-241 phase crystallized at 100 °C and the $La_2O_2SO_4$ and La_2O_2S products calcined from the La-241 at 1200 °C for 1 h in air and N_2/H_2 gas mixture, respectively.

results (Table 1, Fig. 5(c) and (d)). All the above refinements are stable and give well acceptable reliability factors (Table 1, Fig. 5). Refined structural parameters of the four compounds are summarized in Table 1, and the coordinates of atoms and main bond lengths can be found in Tables S1 and S2.

Fig. 6 illustrates crystal structures of the four compounds under discussion. The structure of monoclinic La-241 (space group: $C2/m$), presented in one unit cell (Fig. 6(a)), can be viewed as alternative stacking of sulfate ions and the hydroxide main layer, composed of [LaO_9] polyhedrons, along the a-axis. Among the nine O atoms coordinated to each La center, six are stemming from hydroxyls, two from H_2O molecules, and one from sulfate tetrahedron, and the [LaO_9] presents three-capped trigonal prism in the structure. In monoclinic La-111 (space group: $P2_1/n$), the La center is coordinated with nine surrounding oxygen atoms, three of which come from OH^- and the other six from SO_4^{2-} groups (Fig. 6(b)). $Ln_2O_2SO_4$ may crystallize as one of the two allotropic modifications of monoclinic and orthorhombic systems according to the up to date reports [41,43]. In this work, we found that $La_2O_2SO_4$ has a monoclinic structure (space group: $C2/c$), in which each La is bonded with seven oxygen atoms (three from the SO_4^{2-}) to form one-capped trigonal prism (Fig. 6(c)). This is different from its orthorhombic counterpart [43], where each La is connected with six oxygen atoms to form trigonal prism without any cap. La_2O_2S was found to crystallize in the hexagonal system (P-3m1), where La is bonded with three sulfur and four oxygen atoms to make mono-capped polyhedron of sevenfold coordination (Fig. 6(d)). It is interesting to note that the number of caps is closely related to the coordination number (CN) of La, that is, none cap for CN = 6 in orthorhombic $Ln_2O_2SO_4$, one cap for CN = 7 in monoclinic $Ln_2O_2SO_4$ and hexagonal Ln_2O_2S, and three caps for CN = 9 in both La-241 and La-111. Therefore, trigonal prism seems to be the basic building block for the crystal structure of these compounds, and the coordination number can be increased through cap addition.

By applying the hydrothermal and annealing approaches described above, La-241 separately doped with the important activators of Pr^{3+}, Sm^{3+}, Eu^{3+}, Tb^{3+}, and Dy^{3+} was crystallized at 100 °C (Fig. S3) and phase-pure oxysulfide (Fig. S4) and oxysulfate (Fig. S5) phosphors were successfully derived for luminescent investigations. Particle morphology was not found to be substantially affected by dopant type and content and thus only those of

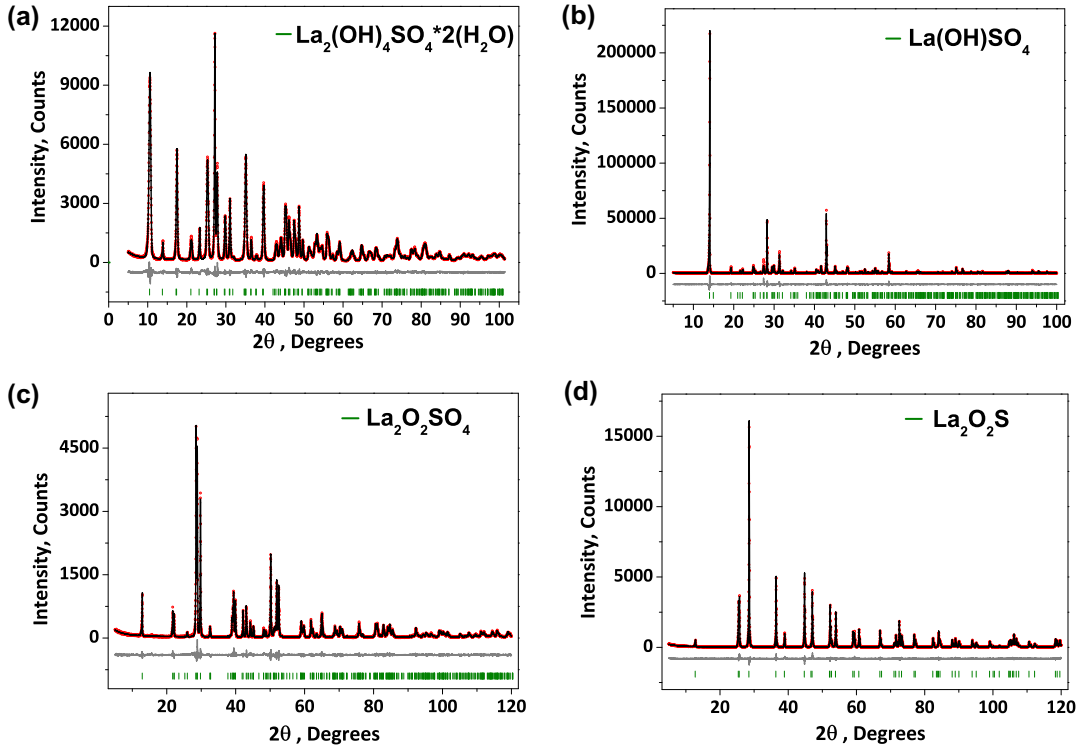

Fig. 5. The observed (black) and calculated (red) XRD profiles and the difference (gray) for La-241 (a), La-111 (b), $La_2O_2SO_4$ (c), and La_2O_2S (d). The Bragg reflections are indicated with green tick marks. (For interpretation of the references to color in this figure legend, the reader is referred to the web version of this article.)

Table 1
Main parameters and results of structure refinement.

Compound	$La_2(OH)_4SO_4{\cdot}2H_2O$	$La(OH)SO_4$	$La_2O_2SO_4$	La_2O_2S
Sp. Gr.	*C*2/*m*	*P*2$_1$/*n*	*C*2/*c*	*P*-3*m*1
a, Å	16.8847(6)	4.5373(1)	14.3446(6)	4.0520(3)
b, Å	3.9420(1)	12.6447(1)	4.2860(2)	4.0520(3)
c, Å	6.4359(2)	6.9853(2)	8.3972(3)	6.9463(6)
β, °	90.454(2)	106.190(2)	106.972(4)	–
V, Å^3	428.36(3)	384.87(1)	493.79(4)	98.770 (2)
Z	2	4	4	1
2*θ*-interval, °	5–100	5–100	5–120	5–120
No. of reflections	273	402	374	76
No. of refined parameters	50	57	48	28
R_{wp} (%)	6.43	13.15	12.12	9.77
R_p (%)	4.68	9.45	8.38	6.57
R_{exp} (%)	4.07	3.08	9.53	7.92
χ^2	1.58	4.27	1.27	1.23
R_B (%)	1.47	4.79	2.31	2.26

Interpretation of reliability factor: R_{wp} for weighted profile reliability factor; R_p for pattern reliability factor; R_{exp} for expected reliability factor; R_B for Bragg reliability factor; χ^2 for goodness of fitting.

the $(La_{0.99}Tb_{0.01})^{3+}$ compounds are presented in Fig. 7 for example. As seen, the platelets in the hydroxyl sulfate precursor (Fig. 7(a)) underwent significant disintegration upon calcination to form rounded particles, whose average crystallite sizes were assayed with Scherrer equation to be ~45 nm. Particle sizing found that the $(La_{0.99}Tb_{0.01})_2O_2S$ and $(La_{0.99}Tb_{0.01})_2O_2SO_4$ phosphors are similarly composed of larger aggregates (~7 μm in average) and much finer particles, whose sizes were averaged to be ~180 nm (~87.5% of the total particles) and ~220 nm (~85% of the total particles), respectively (Fig. S6).

3.2. Photoluminescence investigation of $(La,RE)_2O_2S$ phosphors (RE = Pr, Sm, Eu, Tb, and Dy)

Fig. 8 shows excitation and emission spectra of the different activators in La_2O_2S, with assignments of the electronic transitions labeled in the figures. Pr^{3+} presents broad $4f^2 \rightarrow 4f^1d^1$ inter-configurational excitations in the ~200–350 nm region, with the main peak centered at ~266 nm (Fig. 8(a)). Charge transfer (CT), on the other hand, was found to be the predominant excitation source for Sm^{3+}, Eu^{3+}, and Dy^{3+} in the oxysulfide lattice, which is at ~270 nm for Sm^{3+} (Fig. 8(b)), 264 nm (O–Eu) and 336 nm (S–Eu) for Eu^{3+} (Fig. 8(c)), and 269 nm for Dy^{3+} (Fig. 8(d)). The phosphors exhibit vivid green (Pr^{3+}, 508 nm), red (625 nm for both Sm and Eu), and yellow (Dy^{3+}, 577 nm) emissions under UV excitation, as confirmed by the Commission International de L'Eclairage (CIE) chromaticity coordinates (Fig. S7(a)). Luminescent properties of the phosphors, including main excitation/emission wavelengths, CIE color coordinates, quantum yield (QY), and emission color are tabulated in Table 2.

The PLE spectra of $(La,Tb)_2O_2S$, obtained by monitoring the $^5D_4 \rightarrow {}^7F_5$ transition of Tb^{3+} at 545 nm, were observed to have two parts in each case: a broad and strong band ranging from 250 to 330 nm and much weaker and sharper peaks at longer wavelengths (Fig. 8(e)). Gaussian deconvolution of the broad main excitation (Fig. S8) found three sub-bands centered at ~256, 271, and 303 nm, respectively (Table S6). The bandgap energy of Ln_2O_2S was widely reported to be 4.6–4.8 eV [26,44]. Calculation with the equation $\lambda = 1240/E$, where E is the bandgap energy (eV), yielded wavelength of 258–269 nm, and thus the deconvoluted peak entered at ~256 nm can be assigned to host excitation. The other two peaks located at ~271 and 303 nm are arising from the spin-allowed (LS, $^7F_6 \rightarrow {}^7D_J$) and spin-forbidden (HS, $^7F_6 \rightarrow {}^9D_J$) transitions of Tb^{3+}, respectively [33]. Host excitation is the strongest among the three sub-bands for the low Tb^{3+} concentrations of ⩽1 at.%, and above which $4f^8 \rightarrow 4f^75d^1$ transitions become dominant as expected (Fig. S8). Relative intensity of the LS to HS transitions varies with Tb^{3+} content, since the sensitivity of LS and HS to changes in Tb^{3+} content is different as observed by other researchers [45]. Exciting the $(La,Tb)_2O_2S$ phosphors with the peak

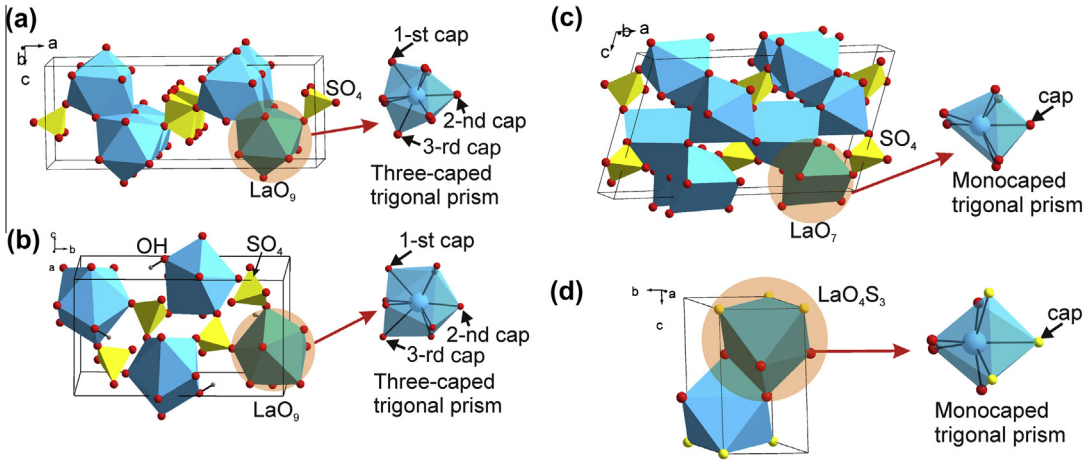

Fig. 6. Crystal structures of La-241 (a), La-111 (b), $La_2O_2SO_4$ (c), and La_2O_2S (d), together with the geometries of polyhedrons.

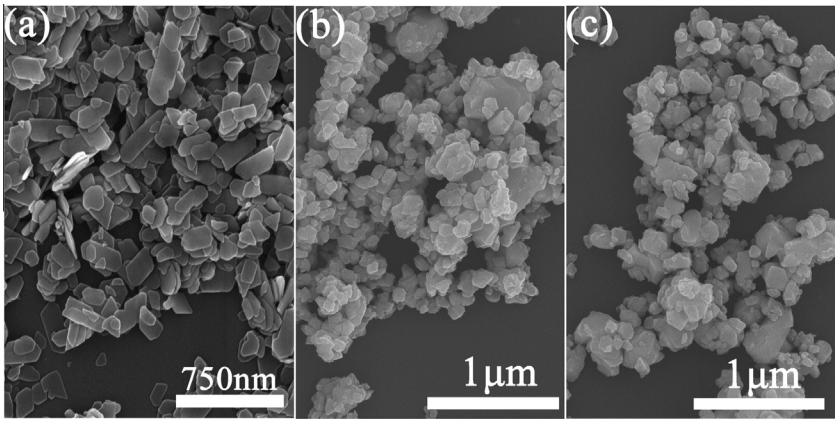

Fig. 7. FE-SEM images of the $(La_{0.99}Tb_{0.01})$-241 precursor (a) and the derived $(La_{0.99}Tb_{0.01})_2O_2S$ (b) and $(La_{0.99}Tb_{0.01})_2O_2SO_4$ (c) phosphors.

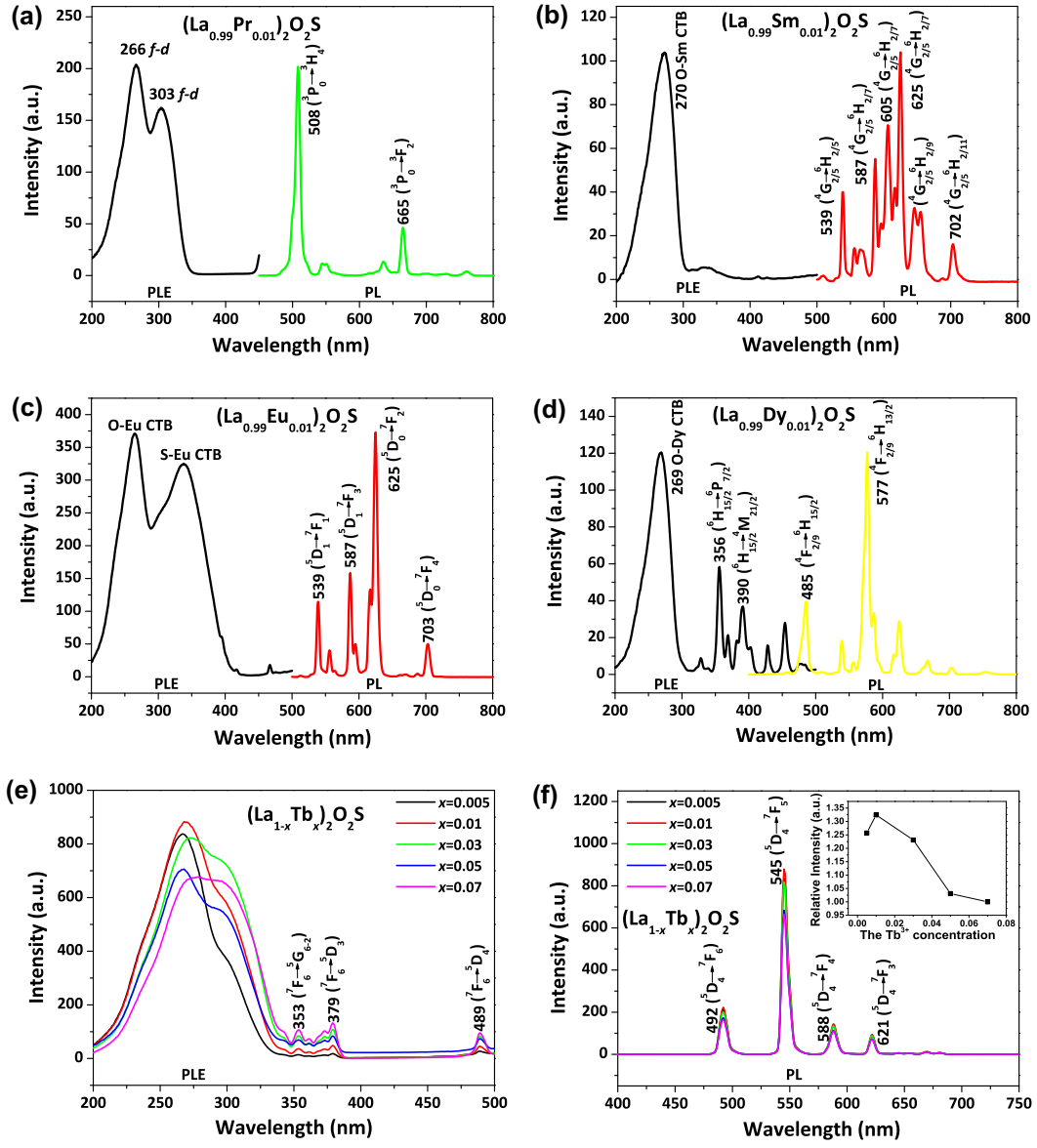

Fig. 8. PLE and PL spectra of the $La_2O_2S:RE^{3+}$ phosphors (RE = Pr, Sm, Eu, Tb, and Dy). Inset in (f) shows intensity evolution of the 545 nm green emission against Tb^{3+} content. (For interpretation of the references to color in this figure legend, the reader is referred to the web version of this article.)

Table 2
A summary of the photoluminescence properties of $(La,RE)_2O_2S$ phosphors.

Sample ID	λ_{ex} (nm)	λ_{em} (nm)	QY	CIE (*x*, *y*)	I_{492}/I_{545}
$(La_{0.99}Pr_{0.01})_2O_2S$	266	508	19.2	(0.15, 0.62)	–
$(La_{0.99}Sm_{0.01})_2O_2S$	270	625	26.2	(0.59, 0.41)	–
$(La_{0.99}Eu_{0.01})_2O_2S$	264	625	48.1	(0.58, 0.42)	–
$(La_{0.99}Dy_{0.01})_2O_2S$	269	577	13.3	(0.45, 0.46)	–
$(La_{0.995}Tb_{0.005})_2O_2S$	268	545	44.2	(0.33, 0.60)	0.256
$(La_{0.99}Tb_{0.01})_2O_2S$	270	545	48.5	(0.33, 0.61)	0.253
$(La_{0.97}Tb_{0.03})_2O_2S$	272	545	46.1	(0.33, 0.61)	0.245
$(La_{0.95}Tb_{0.05})_2O_2S$	270	545	45.8	(0.33, 0.60)	0.253
$(La_{0.93}Tb_{0.07})_2O_2S$	276	545	39.9	(0.33, 0.60)	0.246

wavelengths summarized in Table 2 (also indicated in Fig. S8) similarly produced the $^5D_4 \rightarrow {}^7F_J$ (J = 3–6) emissions of Tb^{3+}, with the $^5D_4 \rightarrow {}^7F_5$ green emission at 545 nm being the strongest.

The optimal Tb^{3+} content was experimentally determined to be ~1 at.% in this work, as shown in the insert of Fig. 8(f). The CIE color coordinates (Table 2, Fig. S7(b)) derived from the PL spectra stay stable at around (0.33, 0.60), corresponding to a vivid green color for all the compositions. The blue to green intensity ratio (I_{492}/I_{545}) keeps almost constant at ~0.25 independent of Tb^{3+} content, and the QY reached its maximum of ~48.5% at 1 at.% of Tb^{3+} (Table 2).

3.3. Photoluminescence investigation of $(La,RE)_2O_2SO_4$ phosphors (RE = Pr, Sm, Eu, Tb, and Dy)

Only recently, $La_2O_2SO_4$ was investigated as an effective host lattice for optical dopants [29], and reports on this type of phosphors are yet rather limited. We thus investigated in this work PL behaviors of the various activators of Pr^{3+}, Sm^{3+}, Eu^{3+}, Tb^{3+}, and Dy^{3+} in $La_2O_2SO_4$, and again the effects of activator content were studied with Tb^{3+}.

Fig. 9 presents excitation and emission spectra of the different activators. $4f^2 \rightarrow 4f^1d^1$ inter-configurational transition centered at ~283 nm, charge transfer transition at 280 nm, intra-$4f^5$ transition at 407 nm ($^6H_{5/2} \rightarrow {}^4K_{11/2}$), and intra-$4f^9$ transition at 350 nm

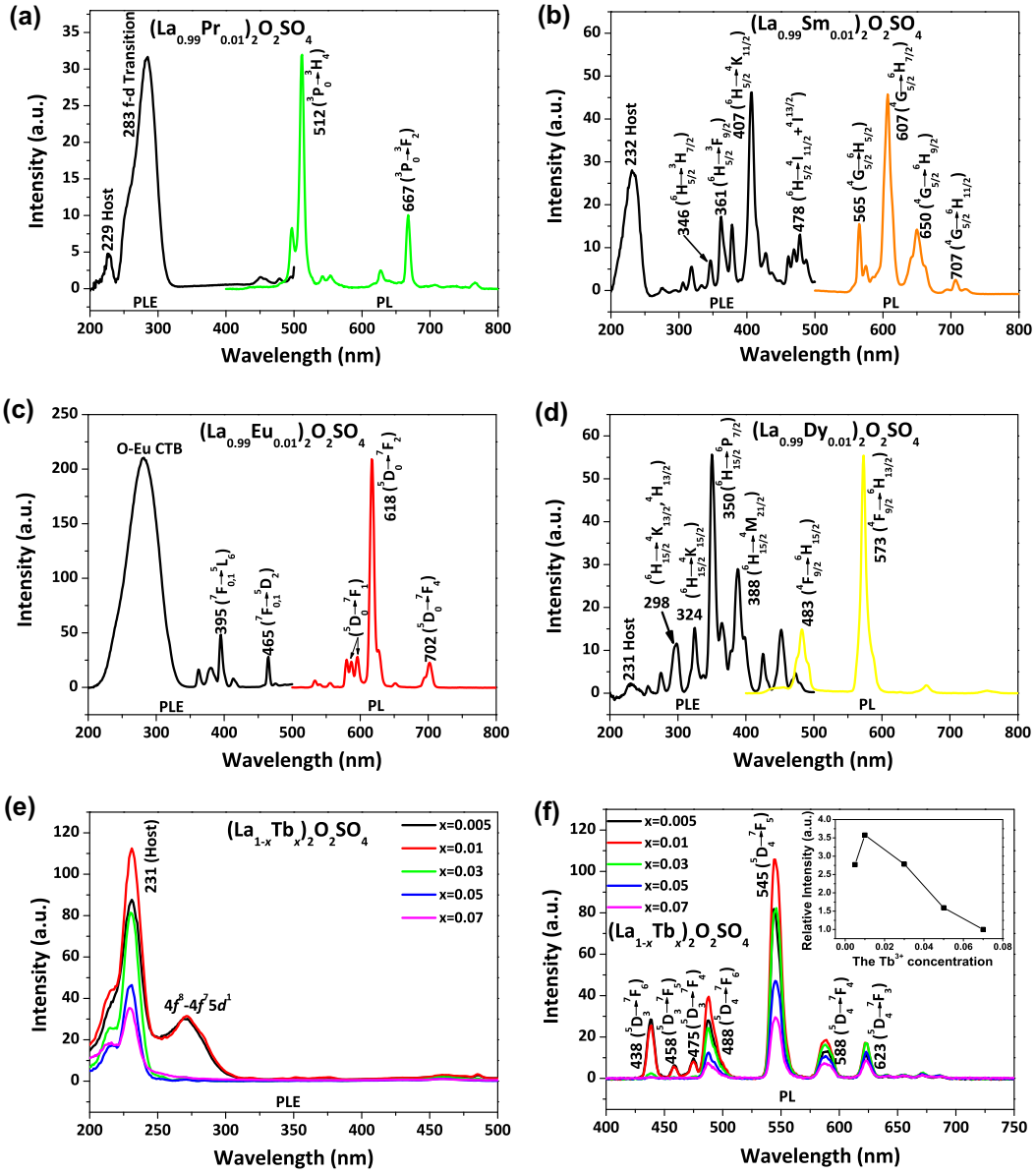

Fig. 9. PLE and PL spectra of the $La_2O_2SO_4$:RE^{3+} phosphors (RE = Pr, Sm, Eu, Tb, and Dy). Inset in (f) shows the intensity evolution of the 545 nm emission as a function of Tb^{3+} content.

Table 3
A summary of photoluminescence properties of the $(La,RE)_2O_2SO_4$ phosphors.

Sample ID	λ_{ex} (nm)	λ_{em} (nm)	CIE (x, y)	QY	I_{488}/I_{545}
$(La_{0.99}Pr_{0.01})_2O_2SO_4$	283	512	(0.19, 0.56)	5.8	–
$(La_{0.99}Sm_{0.01})_2O_2SO_4$	407	607	(0.60, 0.36)	41.7	–
$(La_{0.99}Eu_{0.01})_2O_2SO_4$	280	617	(0.64, 0.36)	27.5	–
$(La_{0.99}Dy_{0.01})_2O_2SO_4$	350	573	(0.39, 0.44)	48.2	–
$(La_{0.995}Tb_{0.005})_2O_2SO_4$	231	545	(0.29, 0.44)	2.2	0.340
$(La_{0.99}Tb_{0.01})_2O_2SO_4$	231	545	(0.30, 0.48)	9.8	0.365
$(La_{0.97}Tb_{0.03})_2O_2SO_4$	231	545	(0.34, 0.55)	6.1	0.295
$(La_{0.95}Tb_{0.05})_2O_2SO_4$	231	545	(0.36, 0.54)	4.3	0.257
$(La_{0.93}Tb_{0.07})_2O_2SO_4$	231	545	(0.37, 0.52)	1.7	0.255

($^6H_{15/2} \rightarrow {}^6P_{7/2}$) were found to be the most efficient excitation sources for Pr^{3+}, Eu^{3+}, Sm^{3+}, and Dy^{3+}, respectively, in accordance with previous reports [46,47]. Under excitation with the above wavelengths, the phosphors produce sharp green (Pr^{3+}, 512 nm), orange (Sm^{3+}, 607 nm), red (Eu^{3+}, 618 nm), and yellow (Dy^{3+}, 573 nm) emissions, as seen from the CIE chromaticity diagram (Fig. S9(a)). The origins of the involved electronic transitions were assigned in each part of the figure and the major properties of the phosphors are summarized in Table 3. The blue to yellow intensity ratio (I_{483}/I_{573}) of Dy^{3+} emission in $La_2O_2SO_4$ is ~0.27, being smaller than that (~0.33) in La_2O_2S. This is due to the fact that the $^4F_{9/2} \rightarrow {}^6H_{15/2}$ blue emission (parity allowed) and the $^4F_{9/2} \rightarrow {}^6H_{13/2}$ yellow emission (parity forbidden) arise from Dy^{3+} taking more and less symmetric lattice sites, respectively [48], while the site symmetry of La (C_1) in $La_2O_2SO_4$ is lower than that (C_{3v}) in La_2O_2S. Nonetheless, the two types of Dy^{3+} sites are generally low in symmetry among all the symmetry groups, and thus the emission is dominated by the yellow band. Fig. 9(e) and (f) illustrate the effects of Tb^{3+} content on $(La,Tb)_2O_2SO_4$ luminescence. The PLE spectra (Fig. 9(e)), obtained by monitoring the 545 nm green emission ($^5D_4 \rightarrow {}^7F_5$), exhibit sharp excitation bands in the 200–250 nm region, with maxima at ~231 nm. The bands may correspond to host excitation as they similarly appear for all the other activators (for Eu^{3+}, the band overlaps the much stronger O–Eu CT band). The broad and much weaker bands at ~270 nm are arising from $4f^8 \rightarrow 4f^7 5d^1$ Tb^{3+} transitions [49], which are completely quenched when the Tb^{3+} content exceeds 1 at.%. The $f \rightarrow d$ excitation quenches much faster in $La_2O_2SO_4$ than in La_2O_2S, possibly due to the fact that the average La–La distance in the former (~4.003 Å) is shorter than that (~4.123 Å) in La_2O_2S. The bandgap energy of $La_2O_2SO_4$ can then be derived to be ~5.3 eV with the equation $\lambda = 1240/E$, which is substantially larger than the 4.6–4.8 eV of Ln_2O_2S [26,44]. The $(La,Tb)_2O_2SO_4$ phosphors show the characteristic blue ($^5D_3 \rightarrow {}^7F_{4-6}$), green ($^5D_4 \rightarrow {}^7F_5$), and red ($^5D_4 \rightarrow {}^7F_{3,4}$) emission bands of Tb^{3+} under 231 nm excitation, with the $^5D_4 \rightarrow {}^7F_5$ (545 nm) green one being overwhelmingly stronger. Again, the optimal Tb content was experimentally found to be ~1 at.% in $La_2O_2SO_4$ (inset, Fig. 9(f)).

It is interesting to note that $La_2O_2SO_4$ differentiates itself from La_2O_2S for Tb^{3+} luminescence, since the latter did not produce any blue emission from the higher-lying $^5D_3$ excited sate. This can be explained from positioning of the excited states of Tb^{3+} in the bandgap of the host lattice. As mentioned before, the bandgap energy of Ln_2O_2S (4.6–4.8 eV) is much lower than that (5.3 eV) of $La_2O_2SO_4$, and thus the bottom of the conduction band of La_2O_2S would lie closer to the $^5D_3$ excited state of Tb^{3+}. In such a case, the $^5D_3$ electrons can be activated to the conduction band under thermal fluctuation and eventually fed to the $^5D_4$ state, leading to complete quenching of $^5D_3$ emission at room temperature [26,33]. The lack of blue component in the emission of $(La,Tb)_2O_2S$ accounts for the constant color coordinates shown in Fig. S7(b). It is also seen that, for $(La,Tb)_2O_2SO_4$, the $^5D_3 \rightarrow {}^7F_{4-6}$ blue emissions are only observable at the low Tb^{3+} contents of up to 3 at.%, above which quenching takes place via cross relaxation between adjacent Tb^{3+} pairs through the equation [26,50]

$$Tb^{3+}(^5D_3) + Tb^{3+}(^7F_6) \rightarrow Tb^{3+}(^5D_4) + Tb^{3+}(^7F_0) \quad (5)$$

The relaxation leads to decreasing intensity ratio of the blue to green emissions (I_{487}/I_{545}, Table 3) at a higher Tb^{3+} content, which explains the varied color coordinates of $(La,Tb)_2O_2SO_4$ (Fig. S9(b)). Quantum yield (QY) of the oxysulfate phosphor reached its maximum of ~9.8% at 1 at.% of Tb^{3+}, corresponding well to intensity evolution of the PL spectra (Fig. 9(f), inset). It was noticed that, under short UV light excitations, the emissions in $La_2O_2SO_4$ have lower quantum efficiencies than in La_2O_2S for the activators of Pr^{3+}, Eu^{3+}, and Tb^{3+}. This is mainly owing to the stronger excitation absorption of La_2O_2S in the UV region, as verified by UV–vis spectroscopy (Fig. S10).

4. Conclusions

Controlled crystallization of $La_2(OH)_4SO_4{\cdot}2H_2O$ layered hydroxyl sulfate (La-241 phase) was achieved under both atmospheric pressure and hydrothermal conditions, through which the two important compounds of La_2O_2S and $La_2O_2SO_4$ were derived via proper calcination, without involving any environmentally harmful substances, for photoluminescence applications. The main findings are summarized as follows:

(1) La-241 can be crystallized via solution reaction in the wide temperature range of RT-120 °C and pH ~ 9. $La(OH)SO_4$ (La-111 phase) crystallizes as a predominant phase in the 150–180 °C range and as a pure phase at 200 °C.
(2) Rietveld structure refinement, first performed for La-241, found that the compound crystallizes in the monoclinic system (space group: $C2/m$) and is isostructural to its Pr–Tb counterparts, but with larger cell parameters and cell volume by the larger size of La^{3+}. Trigonal prism was suggested to be the fundamental building block for the crystal structures of La-241, La-111, $La_2O_2SO_4$, and La_2O_2S, and the number of cap for the prism varies with coordination number of the La center.
(3) The Pr^{3+}, Sm^{3+}, Eu^{3+}, Tb^{3+}, and Dy^{3+} ions in $La_2O_2SO_4$ and La_2O_2S produce green (Pr^{3+} and Tb^{3+}), red (Eu^{3+}), orange red (Sm^{3+}), and yellow (Dy^{3+}) emissions through their characteristic $f \rightarrow f$ transitions under UV excitation, and the effects of host lattice on excitation and emission were revealed.
(4) The optimal concentration of Tb^{3+} was determined to be ~1 at.% for both the oxysulfate and oxysulfide hosts. Cross relaxation was suggested to be responsible for the observed gradual quenching of $^5D_3$ blue emission and thus the decreasing I_{488}/I_{545} ratio and changing color coordinates of the $(La,Tb)_2O_2SO_4$ phosphors, while the lack of $^5D_3$ emission in La_2O_2S was proposed to be due to thermal activation of the $^5D_3$ electrons into the conduction band of the host.

Acknowledgments

This work is supported in part by the National Natural Science Foundation of China (Grants Nos. 51172038, 51302032, and U1302272), the Fundamental Research Fund for the Central Universities (Grant No. N140204002), Grants-in-Aid for Scientific Research (KAKENHI No. 26420686), and the Russian Foundation for Basic Research (15-52-53080). X.J. Wang acknowledges financial support from the China Scholarship Council for her overseas